Comparisons between the WRF model and the GNSS tomography technique in retrieving 3D wet refractivity filed in Hong Kong

Zhaohui Xiong[1], Bao Zhang[1,*] and Yibin Yao[1]

[1] School of Geodesy and Geomatics, Wuhan University, Wuhan 430079;
cehui_xiong@whu.edu.cn (Z.X.); ybyao@whu.edu.cn (Y.Y.)

* Correspondence: sggzb@whu.edu.cn; Tel.: +86-027-6875-8403

Abstract: Water vapor plays an important role in various scales of weather processes. However, there are limited means to monitor its 3-dimensional (3D) dynamical changes. The Numerical Weather Prediction (NWP) model and the Global Navigation Satellite System (GNSS) tomography technique are two of the limited means. Here, we conduct an interesting comparison between the GNSS tomography technique and the Weather Research and Forecasting (WRF) model (a representative of the NWP models) in retrieving Wet Refractivity (WR) in Hong Kong area during a wet period and a dry period. The GNSS tomography technique is used to retrieve WR from the GNSS slant wet delay. The WRF Data Assimilation (WRFDA) model is used to assimilate ZTD to improve the background data. The WRF model is used to generate reanalysis data using the WRFDA output as the initial values. The radiosonde data are used to validate the WR derived from the GNSS tomography and the reanalysis data. The Root Mean Square (RMS) of the tomographic WR, the WRFDA WR that assimilate GNSS ZTD, and the reanalysis WR that without assimilating GNSS ZTD are 6.50 mm/km, 4.31 mm/km and 4.15 mm/km in the wet period. The RMS becomes 7.02 mm/km, 7.26 mm/km and 6.35 mm/km in the dry period. The lower accuracy in the dry period is mainy due to the sharp variation of WR in the vertical direction. The results also show that assimilating GNSS ZTD into the WRFDA model only slightly improves the accuracy of the reanalysis WR and that the reanalysis WR is better than the tomographic WR in most cases. However, in a special experimental period when the water vapor is highly concentrated in the lower troposphere, the tomographic WR outperforms the reanalysis WR in the lower troposphere. When we assimilate the tomographic WR in the lower troposphere into the WRFDA model, the reanalysis WR is improved.

Keywords: GNSS Tomography; Wet Refractivity; Weather Research and Forecasting model; Data Assimilation

1 Introduction

Water vapor (WV), mostly contained in the troposphere, plays an important role in various scales of atmospheric processes. But due to its active nature, there are limited models and techniques that can accurately describe or monitor its 3-dimensional (3D) dynamical changes (Rocken et al., 1993).

The development of Global Navigation Satellite System (GNSS) technique and the densely deployed GNSS receivers provide us the opportunity to monitor the WV filed in near real time. When GNSS signal travels through the neutral atmosphere, it undergoes time delay and bending due to the atmospheric refractivity. This effect is usually called the tropospheric delay in the GNSS field (Altshuler, 2002). The tropospheric delay is usually considered as the product of the zenith delay and the mapping function (Lanyi, 1984; Niell, 1996). The Zenith Tropospheric Delay (ZTD) consists of two parts: the hydrostatic part and the wet part. The wet delay is mainly associated with the WV and reflects WV content in the troposphere. Bevis et al. (Bevis et al., 1992) introduced the principle of using GNSS Zenith Wet Delay (ZWD) to retrieve the Precipitable Water Vapor (PWV). Since then, many scientists carried out the GNSS PWV experiments (Askne and Nordius,1987;

Bokoye et al., 2003; Yao et al., 2014; Lu et al., 2015; Shoji and Sato, 2016). Now, the GNSS PWV can be retrieved with an uncertainty of 1-2 mm in post-processing (Tregoning et al., 1998; Adams et al., 2011; Grejner-Brzezinska, 2013) or real-time modes (Yuan et al., 2014; Li et al., 2014; Li et al., 2015).

The GNSS WV tomography technique was first proposed to monitor the 3D or 4D WV in 2000 (Flores et al., 2000; Seko et al., 2000; Hirahara et al., 2000). Since then, many scientists have proposed refined methods to improve the GNSS WV tomography (Flores et al., 2001; Nilsson and Gradinarsky, 2006; Rohm and Bosy, 2011; Wang et al., 2014; Wang et al., 2014; Zhao and Yao, 2017). The tomographic inversion algorithm can be roughly categorized into two groups. One group solves the tomography equation in the least squares scheme or in the Kalman filter scheme with additional constraints or using a priori information (Flores et al., 2000; Rohm and Bosy, 2011; Cao et al., 2006; Zhang et al., 2017). The other group uses the algebraic reconstruction algorithm or similar methods (Bender et al., 2011; Wang et al., 2014; Zhao and Yao, 2017). Some scientists also use different methods from the above to solve the GNSS WR tomography (Nilsson and Gradinarsky, 2006; Perler et al., 2011; Altuntac, 2015). Besides the algorithm improvement, some scientists tried to optimize the voxel division (Chen and Liu, 2014) or use virtual reference stations (Adavi and Mashhadi-Hossainali, 2014) or use additional GNSS rays (Zhao and Yao, 2017) to increase the effective GNSS rays and thus improve the tomography results. Though the tomography technique has the advantages of (1) free of weather conditions and (2) retrieve 3D WR filed in near real time, it still suffers some problems. The sparse distribution of the GNSS receivers and the bad satellite-receiver geometry lead to serious ill-posed and ill-conditioned problems, and also limit the WR retrieve resolution in both vertical and horizontal domains.

Besides the GNSS tomography technique, the WR can also be retrieved by numerical weather prediction models (Gutman and Bock, 2007; Perler et al., 2011). The Weather Research and Forecasting (WRF) model is a state-of-the-art atmospheric modeling system that is used to simulate the dynamic processes of the atmosphere (Jankov et al., 2005; Carvalhoaabc et al., 2012). It is mainly developed and supported by Mesoscale and Microscale Meteorology (MMM) Laboratory of the National Center for Atmospheric Research. Many studies have demonstrated that assimilating ZTD/PWV into WRF can improve the reanalysis water vapor filed (Pacione et al., 2001; Faccani et al., 2005; Boniface et al., 2012; Bennitt and Jupp, 2012; Moeller et al., 2016; Lindskog et al., 2017). Besides the WRF model, the Japan Meteorological Agency (JMA) Mesoscale Numerical Weather Prediction Model (Nakamura et al., 2004) and AROME NWP system (Boniface et al., 2009) can also make use of ZTD\PWV data assimilation.

Though the GNSS tomography technique and the the WRF model belong to different fileds, Both of them could retrieve 3D WR filed. It will be interesting to compare their capabilities in retrieving WR field under different weather conditions and to explore the feasibility to combine them. Such results may provides insights for the NWP community about this new technique and the possibility of assimilating the tomography results into the NWP models. For the GNSS community, they will get a better understanding of the WRF model and its capability in simulating the water vapor field. For this purpose, we conduct GNSS tomography and data assimilation experiments in Hong Kong area using in Hong Kong SatRef Network in a wet period and a dry period. WR fields retrieved from GNSS tomography and WRF and WRFD outputs are validated by the radiosonde data. We also explore the feasibility of assimilating the GNSS tomographic WR into the WRF model to further improve the WR filed.

2 Research Area and Data Analysis

The study area is within 113.75°E-114.5°E and 22°N-22.6°N as shown in Figure 1. There are 15 continues GNSS stations belonging to the Hong Kong SatRef Network deployed in the study area. They are all equipped with Leica GNSS receivers and antennas to receive the GNSS signals and automatic meteorological devices to record the temperature, pressure, and relative humidity. The average inter-distance between stations is about 10 km. The altitudes of the highest station (HKNP) and the lowest station (HKLM) are 354 m and 10 m.

In GNSS tomography, we regard a network whose altitude differences are less than 1 km as a flat network. Therefore, the SatRef network is vertically flat.

Two periods of GNSS observation data are processed to generate ZTD and Slant Wet Delay (SWD). One is a wet period from July 20 to 26, 2015 when Hong Kong suffered the heaviest daily rainfall of 2015 (191.3 mm rainfall on July 22). The other is a dry period from August 1 to 7, 2015 when Hong Kong is rainless. The details about the GNSS data processing and the SWD reconstruction can be found in Applendix A.

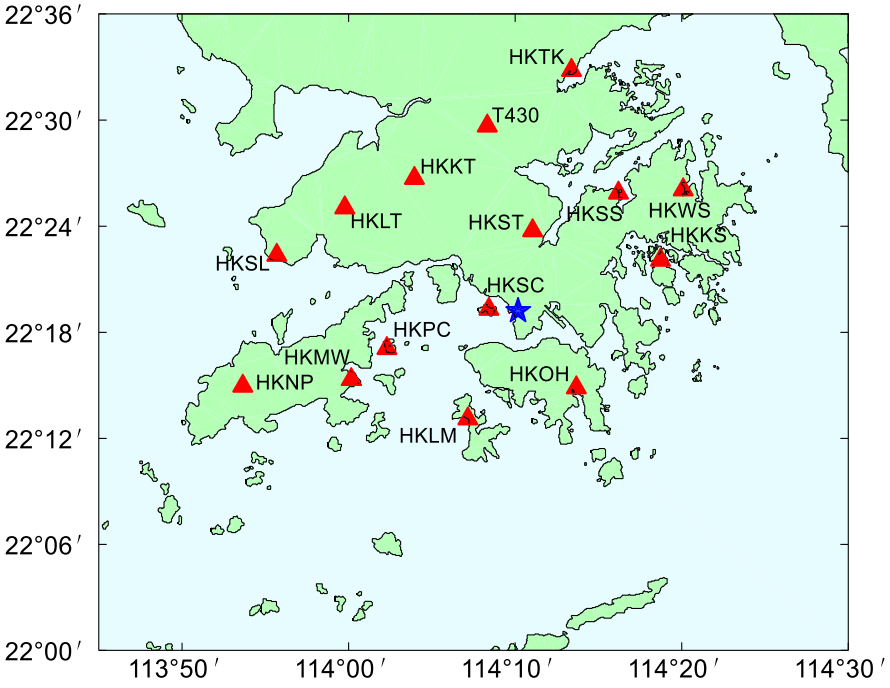

Figure 1. Research area of the experiment. The red triangles indicate the GNSS stations and the blue star indicates the radiosonde station in Hong Kong.

3 Method

3.1. WRF model and Data assimilation

The WRF model version 3.7 is used in this study. The WRFDA-3DVAR is used to assimilate the GNSS ZTD to improve the background data. The WRFDA is designed to obtain the best estimate of the actual atmospheric state at any analysis time (Barker et al., 2004; Huang et al., 2008; Barker et al., 2012; Singh et al., 2017). We use the following settings to run the WRFDA and WRF models. The horizontal resolution of WRFDA and WRF outputs is set to 3 km. And the atmosphere is vertically divided into 45 layers. The pressure of the top layer is 50 hpa. The physics options in this study are unified Noah land-surface model (Tewari et al., 2004), Revised MM5 Monin-Obukhov scheme (Monin and Obukhov, 1954), and Yonsei University planetary boundary layer (PBL) scheme (Hong et al., 2006). There are 10 layers in the PBL. The Rapid Radiative Transfer Model (Mlawer et al., 1997) and Dudhia's scheme (Dudhia, 1989) were used for longwave radiation and shortwave radiation, respectively. The nested mode is not used. This experiment does not apply multiple outer loops and run the 3DVAR once at the beginning of the interested period. We use the ZTD error output by the Bernese 5.0 software. And the start time of the WRF model is epoch of interest.

We use the reanalysis data from European Center for Medium-Range Weather Forecasts (ECMWF) ERA-Interim pressure levels and surface data as the background data, whose spatial resolution is 0.75°× 0.75°. The procedures to do the assimilation experiments are shown in Figure 2.

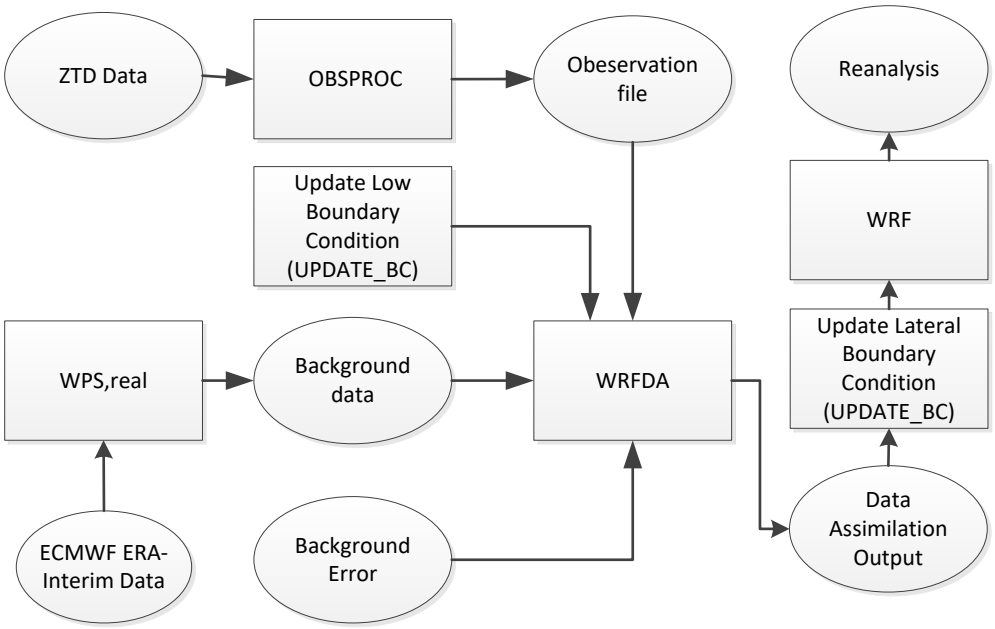

Figure 2. Flowchart of data assimilation using the WRF model.

The background data are processed by WRF preprocessing system (WPS). The WRFDA is run with the generic CV3 option, and the default background error is adopted in this study. The GNSS ZTDs are the input observations for WRFDA. We run WRFDA and obtain the output which is then used to initialize the WRF model. For comparison's sake, we also run the WRF model using the WRFDA output that assimilates nothing as the initial conditions.

When we obtain the outputs from the WRFDA and WRF model, we use Equation (1) to calculate WR (Vedel and Huang, 2004).

$$WR = \frac{P_w}{T} \times (k_1 + \frac{k_2}{T}) \tag{1}$$

where P_w is the water vapor pressure in each grid point in Pascal, T is the temperature in each grid point in Kelvin. k_1= 2.21×10^{-7} K/Pa, k_2 = 3.73×10^{-3} K²/Pa. We use Equation (2) to calculate P_w from reanalysis data.

$$P_w = \frac{p \times q}{0.622} \tag{2}$$

where ***p*** is the pressure in Pascal, ***q*** is the specific humidity in g/g.

3.2. GNSS tomography

The limited number of stations, flat vertical distribution of stations, and bad satellite-station geometry impose serious ill-posed problem in the WR tomography. To well handle this problem, we use the tomography method proposed by Zhang et al. (2017). This method is based on the adaptive Laplacian smoothing and Helmert Variance Component Estimation. It also uses the meteorological data from each GNSS station to constrain the WR near the ground. This tomography strategy is free of a priori information, which makes it an independent technique and thus ensures the fairness when the tomography technique is compared with the WRF model. The WR can be retrieved directly by this tomography strategy when the SWDs are used as

observations. The troposphere is vertically divided into 13 layers with a constant thickness of 800 meters, and horizontally divided into grids whose resolution is ~10 km in longitudinal direction and ~8 km in latitudinal direction. The tomography algorithm is described as follows:

$$\left.\begin{aligned} \mathbf{Y} &= \mathbf{AX} \\ \mathbf{0} &= \mathbf{VX} \\ \mathbf{0} &= \mathbf{HX} \\ \mathbf{0} &= \mathbf{BX} \\ \mathbf{X}_m &= \mathbf{X} \end{aligned}\right\} \tag{3}$$

where the first equation is the observation equation, $\mathbf{Y}$ is the vector of SWDs, $\mathbf{A}$ is the design matrix consisting of intercepts in each voxel, $\mathbf{X}$ is the vector of WR in each voxel. The second to the forth equations in Equation (3) are the vertical, horizontal, and boundary constraints. The fifth equation is used to constrain the WR near the ground using the meteorological data at each GNSS station. $\mathbf{V}$, $\mathbf{H}$, and $\mathbf{B}$ are design matrix for constraint equations. The boundary constraints are established by setting the WR in the top layer to 0. The vertical and horizontal constraints are established by Laplacian smoothing in the vertical and horizontal directions, respectively. The Laplacian smoothing can be described as:

$$x_1 + x_2 + x_3 + x_4 - qx_0 = 0 \tag{4}$$

where the WR x_0 equals the weighted average WR of its nearest four voxels in the same plane, q is the smoothing factor.

In a least square scheme, the solution can be found by:

$$\mathbf{X} = (\mathbf{A}^{\mathrm{T}}\mathbf{A} + \lambda_1\mathbf{V}^{\mathrm{T}}\mathbf{V} + \lambda_2\mathbf{H}^{\mathrm{T}}\mathbf{H} + \lambda_3\mathbf{B}^{\mathrm{T}}\mathbf{B} + \lambda_4)^{-1}(\mathbf{A}^{\mathrm{T}}\mathbf{Y} + \lambda_4\mathbf{X}_m) \tag{5}$$

Where l_i (i = 1, 2, 3, 4) are the weights of corresponding constraints.

In Zhang et al. (2017), the solution is found in an iterative feedback-update process, which is be simply described as follows:

(a) Establish the initial constraints and initialize their weights as 1, namely $\lambda_1 = \lambda_2 = 1$. λ_3 is set to a large value, λ_4 is set to 1; λ_3 and λ_4 are not updated in the following run.

(b) Determine the values of λ_1 and λ_2 by Helmert Variance Component Estimation method and calculate the tomography solutions by Equation (5);

(c) Update the smoothing factors by using the solutions in (b):

$$q = \begin{cases} n & \text{if} \quad x_0 < x_m \\ \dfrac{\sum_{i=1}^{n} x_i}{x_0} & \text{if} \quad x_0 > x_m \end{cases} \tag{6}$$

where n is the number of voxels used to calculate the weighted average. x_m is a threshold set to prevent updating the smoothing factor by inaccurate solutions. The initial value for x_m is half of the maximum wet

refractivity in the solutions. x_m is updated by multiplying x_m by a scale factor, say 0.9, after each run until it is no larger than 3 times the mean square error of $\mathbf{X}$.

(d) Use the new smoothing factors in (c) to update the horizontal and vertical constraints and redo (b) and (c) until the mean square error of the solution differences between this run and the previous run approaches a stable value. In practice, we set a threshold of 20 iterations which is enough to ensure a stable solution.

4 Results

The radiosonde data are used to validate the WR derived from GNSS tomography and the outputs of WRFDA and WRF. Since the radiosonde launches at 0:00 and 12:00 UTC daily, the WR at these epochs are validated. Equation (1) is also used to calculate WR from radiosonde data. The vertical coordinates of WRF model output are converted to geopotential heights by NCL and the geodetic heights of tomographic results are converted to normal height. The slight differences between geopotential heights and normal heights are neglected. We interpolate the WRF output to tomographic nodes since the former has a much higher resolution ~23 layers from 0 to 10 km height) than the latter (13 layers) and thus we can get a higher interpolation accuracy. We use a bi-linear interpolation method in the horizontal domain and a linear interpolation method in the vertical direction. By these methods, we interpolate both the WRF output and radiosonde results to the tomography nodes. Finally, the WR from the outputs of WRFDA and WRF and GNSS tomography are validated by the radiosonde data. For simplicity, WR from radiosonde data, WRFDA output that assimilate ZTD, WRF output that without assimilating GNSS ZTD, and GNSS tomography are denoted as “Radiosonde”, “Reanalysis1”, “Reanalysis2”, and “Tomography” hereinafter.

Figures 3 and 4 show the vertical profiles of the Radiosonde, the Reanalysis1, the Reanalysis2, and the Tomography in the July and August periods, respectively. The Reanalysis1, Reanalysis2, and Tomography agree well with the Radiosonde, which indicates that these three methods successfully retrieved the vertical profile of the WR. It is also observed that the Reanalysis1, the Reanalysis2, and the Tomography agree better with the Radiosonde in the July period than in the August period. This difference should be due to the vertical distribution of WR. Though Hong Kong suffered heavy rain in the July period, the WR was more evenly distributed from 0 to 10 km height than that in the August period. In the dry August period, the WR was highly concentrated in the lower troposphere (< 6 km) and its vertical changes were very sharp. This situation decreased the performance of the tomography technique and the WRF model. This also indicate that both methods have decreased capabilities in retrieving WR in highly changing troposphere. Compared with Reanalysis2, the Reanalysis1 is slightly improved by reducing the mean absolute error (MAE) by 1.25 mm/km. The difference between the Tomography and the Reanlysis1 is obvious at some time epochs in the dry period (e.g., 12:00 on August 4 and 5).

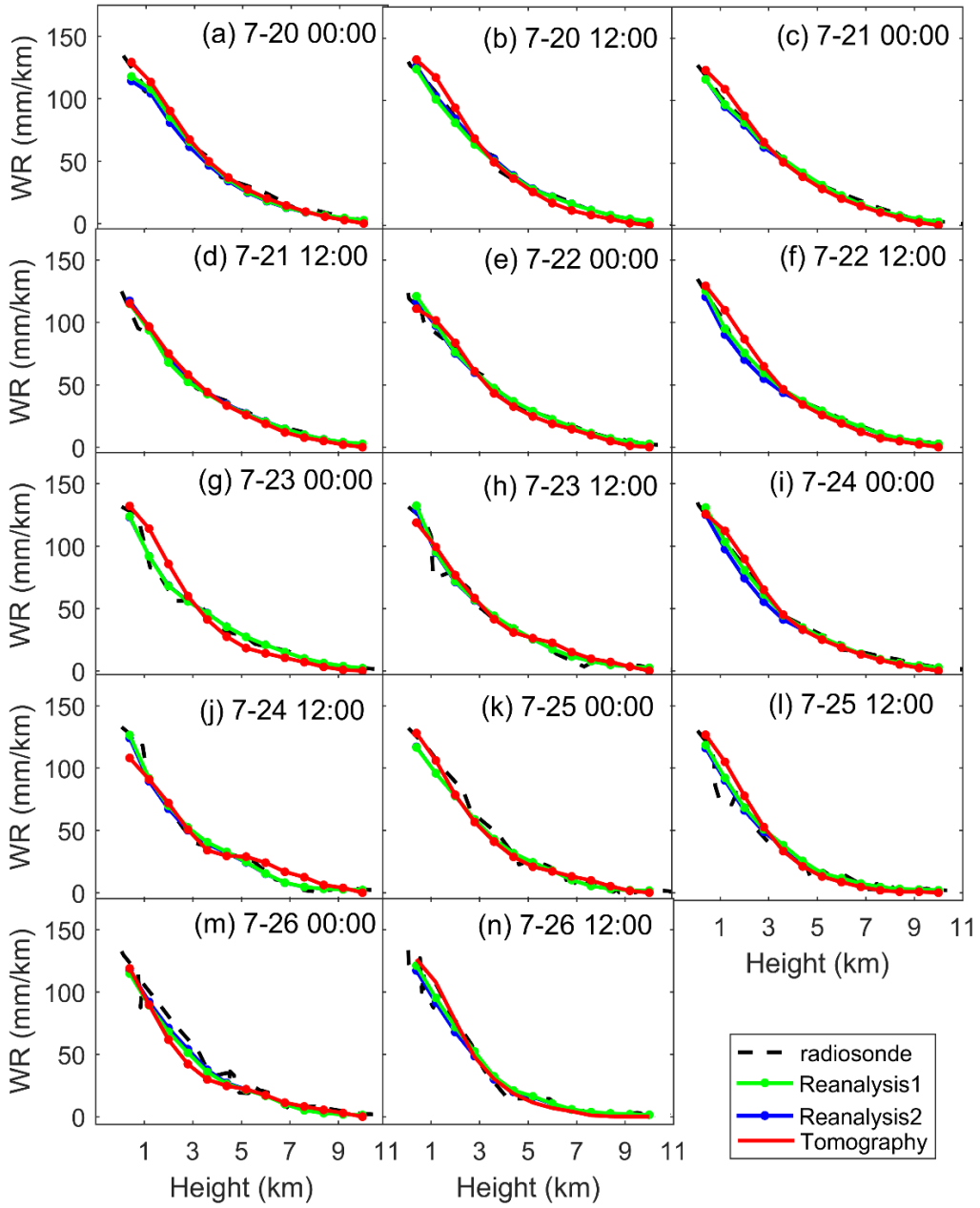

194
195 **Figure 3.** Comparisons among WR derived from reanalysis, tomography, and radiosonde in the wet period,
196 2015.

197

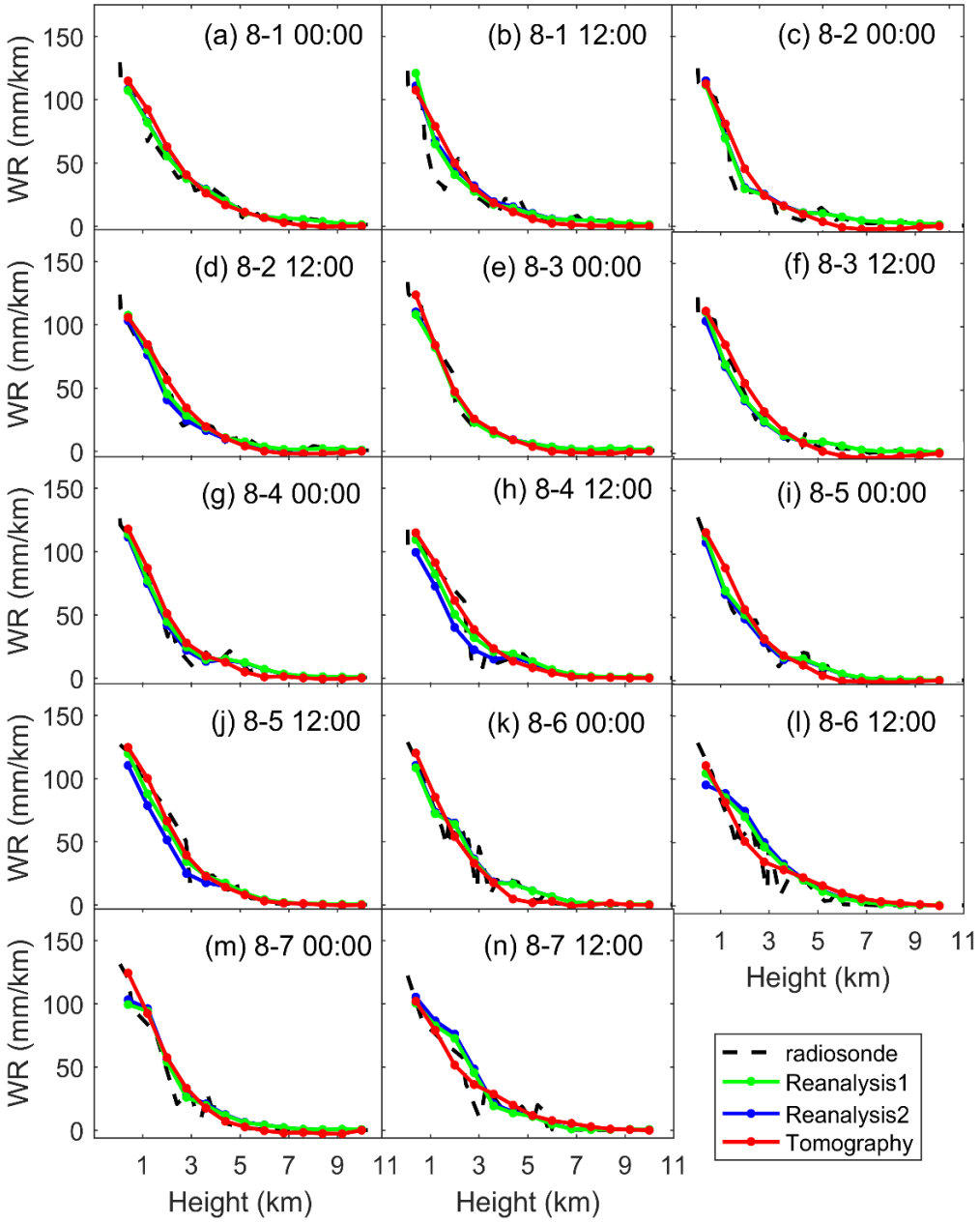

Figure 4. Comparisons among WR derived from reanalysis, tomography, and radiosonde in the dry period, 2015.

Figure 5 shows the statistics of the bias, standard deviation (STD), and Root Mean Square (RMS) of the Tomography, the Reanalysis1, and the Reanalysis2 validated by the Radiosonde at different heights. In the wet period, bias of Reanalysis1 is smaller than that of Reanalysis2, but the differences are not obvious in terms of STD and RMS. In the dry period, the bias of Reanalysis1 in the lower troposphere is slightly greater than that of the Reanalysis2. Overall, the differences between Reanalysis1 and Reanalysis2 are not significant.

In the wet period, the bias, STD, and RMS of the Tomography are greater than that of the Reanalysis1 in most of the time. But in the dry period, the STD and RMS of the Tomography tend to be smaller than that of the Reanalysis1 in the lower troposphere, but its bias is still greater. In general, the WRF model performs better than the tomography technique in most of the cases, but the RMS of Tomography validated by the Radiosonde in 400 m, 1600 m and 2400 m height is smaller than Reanalysis1 as shown in Figure 5f. So, in the lower troposphere in the dry period the tomography performed better than the WRF model in terms of RMS.

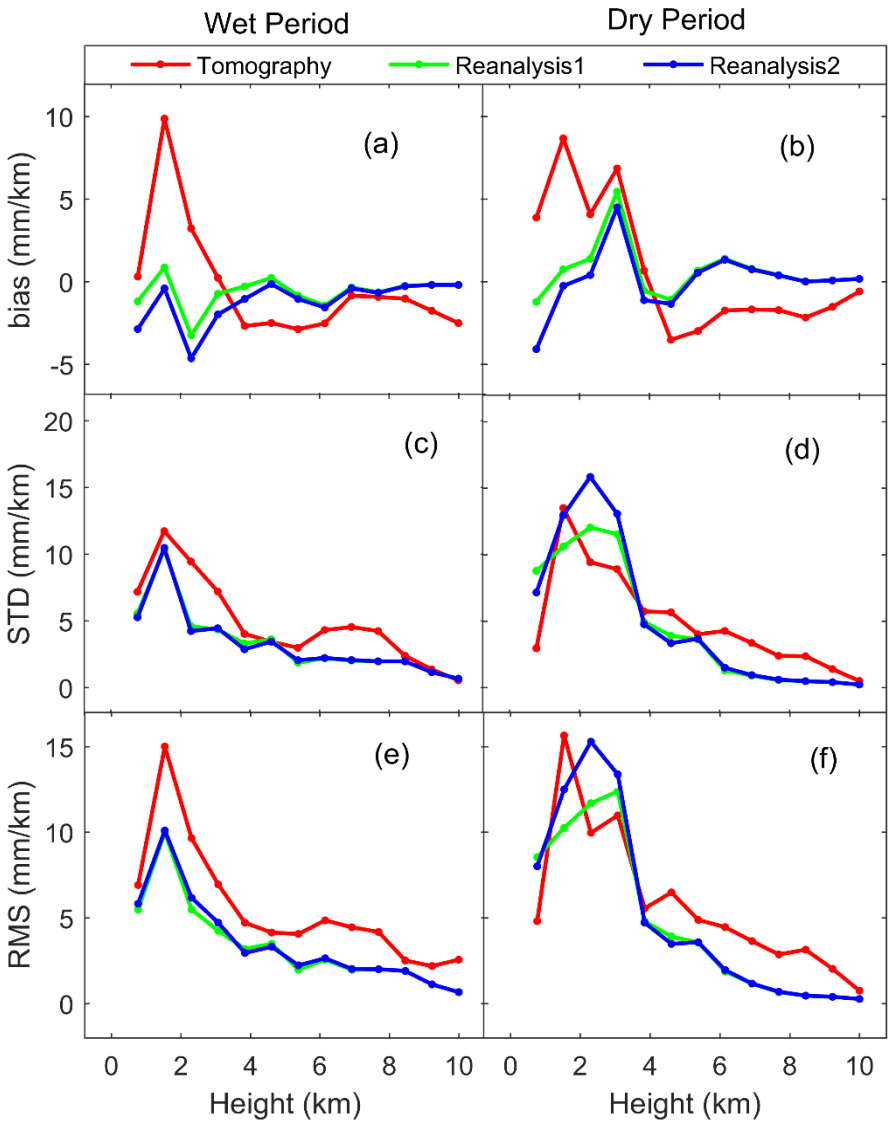

212

213 **Figure 5.** Statistics of bias, STD, and RMS of Tomography, Reanalysis1, and Reanalysis2 validated by the
214 Radiosonde.

215 Table 1 shows the bias, STD, and RMS of Tomography, Reanalysis1, and Reanalysis2 validated by the
216 Radiosonde. In the whole troposphere in the wet period, Tomography has the smallest bias but the largest
217 STD and RMS. The Reanalysis1 and Reanalysis2 have the similar STD and RMS that are much smaller than
218 that of the Tomography. But the Reanalysis2 has the largest bias than Reanalysis1 and the Tomography. In
219 the lower troposphere in the wet period, Reanalysis1 has the smallest STD and RMS while the Tomography
220 has the largest ones. The bias of Tomography is positive in the low troposphere but negative in the upper
221 troposphere, this should be due to the vertical smoothing constraints imposed on the WR. In the upper
222 troposphere in the wet period, Tomography has the largest bias, STD, and RMS while Reanlysis1 has the
223 smallest ones. Overall, both the tomography and the reanalysis results have larger bias, STD, and RMS in the
224 lower troposphere than in the upper troposphere, indicating both the tomography technique and the WRF
225 model has deceased capabilities in the lower troposphere.

226 In the whole troposphere in the dry period, Reanalysis2 has the smallest bias but the largest STD and RMS.
227 The STD and RMS of Tomography are larger than Reanalysis1. In the lower troposphere in the dry period,
228 Reanalysis2 has the largest RMS and STD while Reanalysis1 has the smallest ones. In the low troposphere in
229 the dry period, the performance of Tomography is not as good as Reanalysis1 in terms of RMS. However, in

the upper troposphere in the dry period, the Tomography has relatively larger bias, STD and RMS than the reanalysis results.

Table 1. Statistics of bias, RMS and STD of Tomography, Reanalysis validated by the radiosonde WR. Unit is mm/km.

		Wet Period			Dry Period		
		bias	**STD**	**RMS**	**bias**	**STD**	**RMS**
Total	Reanalysis1	-0.64	4.11	4.15	0.63	6.34	6.35
	Reanalysis2	-1.19	4.15	4.31	0.10	7.28	7.26
	Tomography	-0.31	6.51	6.50	0.63	7.01	7.02
Low (< 5.6 km)	Reanalysis1	-0.74	5.37	5.40	0.77	8.62	8.61
	Reanalysis2	-1.73	5.37	5.62	-0.19	9.90	9.85
	Tomography	0.80	8.20	8.19	2.52	8.83	9.13
Upper (≥ 5.6 km)	Reanalysis1	-0.51	1.75	1.81	0.47	0.86	0.97
	Reanalysis2	-0.55	1.77	1.84	0.45	0.91	1.01
	Tomography	-1.60	3.26	3.62	-1.57	2.63	3.05

In general, assimilating GNSS ZTD into the WRF model has slightly improved the WR retrieval by decreasing the RMS by 0.2 mm/km. The WR derived from Reanalysis1 and Reanalysis2 has apparently smaller RMS than the tomographic WR (4.15 mm/km vs. 6.50 mm/km and 4.31 mm/km vs. 6.50 mm/km, respectively). The results obtained from WRF and tomography are better in the wet period than in the dry period, which is mainly due to the sharp vertical variation of WR in the dry period.

5 Discussion

In the dry period, due to the sharp vertical variations of WR, the Tomography, the Reanalysis have decreased performance in retrieving the WR, especially in the lower troposphere. Compared with the results in the wet period, the RMS of the Tomography and the Reanalysis1 increases by 0.94 mm/km, 3.24 mm/km in the dry period, respectively. The accuracy decrease is more significant in the Reanalysis1 than in the Tomography, resulting in that the tomographic WR becomes better than the reanalysis WR (Figures 5d and 5f) in the low troposphere.

When assimilating ZTD into the WRFDA, we only use the total water vapor and cannot use the vertical profile of water vapor. This leads to that the assimilation of ZTD has limited improvement in retrieving the vertical structure of the WR. Therefore, it is natural to consider assimilating the tomographic WR into the WRFDA to improve the retrieval of the vertical structure of WR. At present, WRFDA could not assimilate WR directly, but can assimilate meteorological parameters such as relative humidity, temperature and pressure. To assimilate the tomographic WR, we convert WR to relative humidity.

The relationship between relative humidity (*RH*) and P_w is shown as Equation (7).

$$RH = \frac{P_w}{P_s} \tag{7}$$

where P_s is the saturated water vapor pressure which is related to temperature and can be calculated by Wexler formula (Wexler, 1976,1977). The P_w is calculated by Equation (1). The needed temperature and pressure data are from the WRF output that assimilate nothing.

After converting the tomographic WR to *RH*, we assimilate the *RH* together with the corresponding temperature and pressure into the WRFDA. Then, the similar procedures as described in Section 3.1 are performed to generate reanalysis.

The Tomography agrees better with the Radiosonde than the Reanalysis1 and Reanalysis2 in the lower troposphere below 3 km at 12:00 on August 6 (Figure 4l) and at 12:00 on August 7 (Figure 4n). So, we assimilate the tomographic WR below 3 km into the WRFDA at these two epochs. The generated reanalysis data are denoted as "Reanalysis3". The difference between Reanalysis3 and Radiosonde is denoted as "DA-Tomo". The difference between Reanalysis1 and Radiosonde is denoted as "DA-ZTD". The difference between Tomography and Radiosonde is denoted as "Tomo". The MAE at different heights at 12:00 on August 6 and 7 are shown in Figure 6.

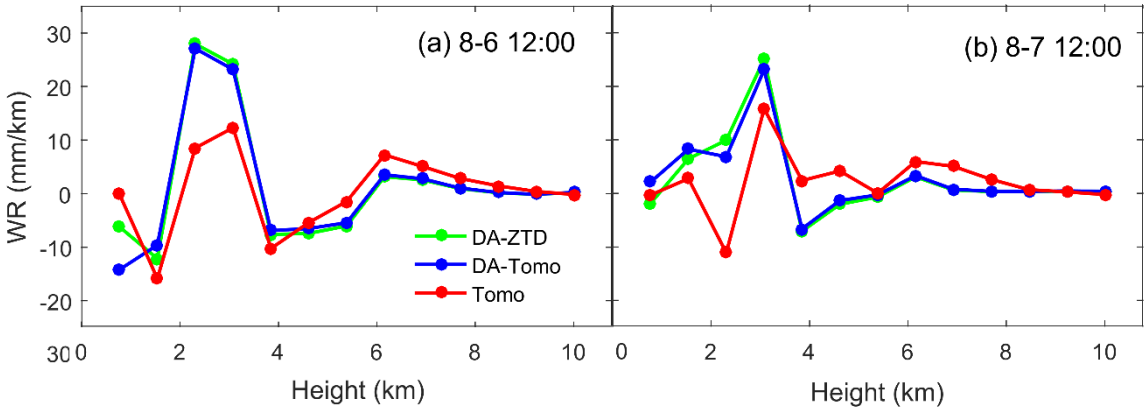

Figure 6. Differences between WR obtained by various methods and radiosonde WR.

Figure 6 shows that the DA-ZTD is very close to the DA-Tomo. The MAE of DA-ZTD is 6.04 mm/km and the MAE of DA-Tomo is 5.92 mm/km. This indicates that assimilating tomographic WR into the WRF model can slightly improve the WR retrieve. But the large uncertainty (8.35 mm/km) of tomography WR in the lower troposphere limit the improvement.

6 Conclusions

GNSS WR tomography and data assimilation experiments are conducted in Hong Kong during a wet and a dry period to test the capabilities of the tomography technique and the WRF model in retrieving WR. The results show that both the tomography technique and the WRF model can retrieve WR that agrees well with the radiosonde data.

In the wet period in the whole troposphere, the RMS of Tomography, Reanalysis1 and Reanalysis2 are 6.50 mm/km, 4.31 mm/km, and 4.15 mm/km. The RMS becomes 7.02 mm/km, 6.35 mm/km, and 7.26 mm/km in the dry period. Both methods obtained better WR in the wet period than in the dry period. We infer that the sharp vertical variations of WR reduced the WR retrieving accuracy in the dry period. In most of the cases, the reanalysis WR outperforms the tomographic WR but the tomographic WR is better than the reanalysis WR in the lower troposphere in the dry period. By assimilating better tomographic WR in the lower troposphere into the WRFDA model, we slightly improve the reanalysis WR.

The above results suggest that both the WRF model and the tomography technique can retrieve good WR but also have drawbacks. If we combine the two by assimilating good tomographic WR into the WRFDA, we may further improve the performance of the WRF model in retrieving the water vapor field.

Data availability. All the data used in this paper are available upon request by email (sggzb@whu.edu.cn).

Appendix A

The GNSS observation data are processed by the precise point positioning module in Bernese 5.0 software using the same settings as detailed in Zhang et al. (2017). The International GNSS Service final orbit and clock products are used. The differential code Biases (DCB) is corrected by products from the Center for Orbit Determination in Europe. Antenna phase center offsets and variations, phase wind-up, Earth tides, Earth rotation, ocean tides and relativistic effects are corrected by conventional methods detailed in (Kouba and Héroux, 2001). We use the ionosphere-free combination of double frequencies to eliminate the first order ionospheric delay and the higher-order terms are ignored. The tropospheric delay models are Saastamoinen model (Saastamoinen, 1972) and Niell mapping functions (Niell, 1996). The cut-off elevation angle is 10°. The station coordinates and ZTDs are estimated simultaneously. Accurate zenith hydrostatic delays (ZHD) are estimated by using the in-situ pressure observations and Saastamoinen model. The ZWD is estimated by removing the ZHDs from the corresponding ZTDs. The SWD is reconstructed by mapping the ZWD and horizontal gradients onto the ray direction. The phase residuals are added to SWD to consider the inhomogeneity of the troposphere.

Conflicts of Interest. The authors declare no conflict of interest.

Acknowledgments. The authors would like to thank the Survey and Mapping Office/Lands Department of Hong Kong, IGRA, and ECMWF for providing experimental data, and thank Mesoscale and Microscale Meteorology Laboratory of the National Center for Atmospheric Research for providing WRF model. This research is funded by the National Science Foundation of China (41704004; 41574028) and supported by Key Laboratory of Geospace Environment and Geodesy, Ministry of Education, Wuhan University (17-02-03).

References

Adams, K.; Fernandes, S.; Maia, F. GNSS Precipitable Water Vapor from an Amazonian Rain Forest Flux Tower. Journal of Atmospheric & Oceanic Technology, 28(10):1192-1198, doi: 10.1175/jtech-d-11-00082.1, 2011.

Adavi, Z; Mashhadi-Hossainali, M. 4D tomographic reconstruction of the tropospheric wet refractivity using the concept of virtual reference station, case study: northwest of Iran. M. Meteorol Atmos Phys, 126(3-4): 193-205. doi:10.1007/s00703-014-0342-4,2014.

Altshuler E E. Tropospheric range-error corrections for the Global Positioning System. IEEE Transactions on Antennas & Propagation, 46(5):643-649, doi: 10.1109/8.668906, 2002.

Altuntac, E. Quasi-Newton Approach for an Atmospheric Tomography Problem. eprint arXiv:1511.08022, Available at: https://arxiv.org/pdf/1511.08022.pdf (accessed on 4 May 2018) , 2015.

Askne, J.; Nordius, H. Estimation of Tropospheric Delay for Microwaves from Surface Weather Data. Radio Sci., 22(3): 379-386, doi: 10.1029/rs022i003p00379, 1987.

Barker, D.; Huang, Y.; Liu, Z.; Auligné, T.; Zhang, X.; Rugg, S.; Demirtas, M. The weather research and forecasting model's community variational/ensemble data assimilation system: WRFDA. Bulletin of the American Meteorological Society,93(6), 831-843, doi: 10.1175/BAMS-D-11-00167.1, 2012.

Barker, M.; Huang, W.; Guo, R.; Bourgeois, J.; Xiao, N. A three-dimensional variational data assimilation system for MM5: Implementation and initial results. Monthly Weather Review, 132(4), 897-914, doi: 10.1175/1520-0493(2004)132<0897:ATVDAS>2.0.CO;2, 2004.

Bender, M.; Dick, G.; Ge, M.; Deng, Z.; Wickert, J.; Kahle, G.; Tetzlaff, G. Development of a GNSS water vapour tomography system using algebraic reconstruction techniques. Advances in Space Research, 47(10): 1704-1720, doi: 10.1016/j.asr.2010.05.034, 2011.

Bennitt, V.; Jupp, A. Operational assimilation of GPS zenith total delay observations into the Met Office numerical weather prediction models. Monthly Weather Review, 140(8), 2706-2719, doi:10.1175/MWR-D-11-00156.1, 2012.

Bevis, M.; Businger, S.; Herring, A.; Rocken, C.; Anthes, A.; Ware, H. GPS meteorology: remote sensing of atmospheric water vapor using the global positioning system. J. Geophys. Res., 97(D14): 15,787-15,801, doi: 10.1029/92JD01517, 1992.

Bokoye, I.; Royer, A.; O'Neill, T.; Cliche, P.; McArthur, B.; Teillet, M.; Thériault, M.. Multisensor analysis of integrated atmospheric water vapor over Canada and Alaska. J. Geophys. Res., 108(D15): 4480, doi: 10.1029/2002jd002721, 2003.

Boniface, K.; Ducrocq, V.; Jaubert, G.; Yan, X.; Brousseau, P.; Masson, F.; Doerflinger, E. Impact of high-resolution data assimilation of GPS zenith delay on Mediterranean heavy rainfall forecasting. Annales Geophysicae, 27: 2739-2753, doi:10.5194/angeo-27-2739-2009, 2009.

Cao, Y.; Chen, Y.; Pingwha, I. Wet Refractivity Tomography with an improved Kalman-Filter Method. Advances in Atmospheric Sciences, 23(5):693-699, doi: 10.5194/angeo-35-87-2017, 2006.

Carvalhoaabc, D. A sensitivity study of the WRF model in wind simulation for an area of high wind energy. Environmental Modelling & Software, 33(7):23-34, doi:10.1016/j.envsoft.2012.01.019, 2012.

Chen, B.; Liu, Z. Voxel-optimized regional water vapor tomography and comparison with radiosonde and numerical weather mode. J Geod, 88, 691–703,doi: 10.1007/s00190-014-0715-y, 2014.

Dudhia, J. Numerical Study of Convection Observed during the Winter Monsoon Experiment Using a Mesoscale Two-Dimensional Model. J.atmos., 46(46): 3077-3107, doi: 10.1175/1520-0469(1989)046<3077:nsocod>2.0.co;2, 1989.

Faccani, C.; Ferretti, R.; Pacione, R.; Paolucci, T.; Vespe, F.; Cucurull, L. Impact of a high density GPS network on the operational forecast. Advances in Geosciences, 2, 73-79, doi:10.5194/adgeo-2-73-2005, 2005.

Flores, A.; De Arellano, G.; Gradinarsky, P.; Rius, A. Tomography of the Lower Troposphere Using a Small Dense Network of GPS Receivers. IEEE Transactions on Geoscience and Remote Sensing, 39(2): 439-447, doi: 10.1109/36.905252, 2001.

Flores, A.; Ruffini, G.; Rius, A. 4D tropospheric tomography using GPS slant wet delays. Annales Geophysicae, 18(2):223-234, doi: 10.1007/s005850050025, 2000.

Grejner-Brzezinska, A. GPS-PWV estimation and validation with radiosonde data and numerical weather prediction model in Antarctica. Gps Solutions, 17(1):29-39, doi: 10.1007/s10291-012-0258-8, 2013.

Gutman, I.; Bock, Y. Tropospheric Signal Delay Estimates Derived from Numerical Weather Prediction Models and Their Impact on Real-Time GNSS Positioning Accuracy. AGU Fall Meeting, San Francisco ,USA, 10-14 December 2007.

Hirahara, K. Local GPS tropospheric tomography. Earth Planets & Space, 52(11):935-939, doi: 10.1186/bf03352308, 2000.

Hong, Y.; Noh, Y.; Dudhia, J. A New Vertical Diffusion Package with an Explicit Treatment of Entrainment Processes. Monthly Weather Review, 134(9):2318, doi: 10.1175/MWR3199.1, 2006.

Huang, Y.; Xiao, Q.; Barker, M.; Zhang, X.; Michalakes, J.; Huang, W.; Dudhia, J. Four-Dimensional Variational Data Assimilation for WRF: Formulation and Preliminary Results. Monthly Weather Review, 137(1):299-314, doi:10.1175/2008MWR2577.1, 2008

Jankov, I.; Gallus Jr.; W. A.; Segal, M.; Shaw, B.; Koch, E. The Impact of Different WRF Model Physical Parameterizations and Their Interactions on Warm Season MCS Rainfall. Weather & Forecasting, 20(6):1048-1060, doi:10.1175/WAF888.1, 2005.

Kouba, J.; Héroux, P., Precise point positioning using IGS orbit and clock products. GPS Solut. 5, 12-28, doi:10.1007/PL00012883, 2001.

Lanyi, G. Tropospheric delay effects in radio interferometry. Telecommunications & Data Acquisition Progress Report, 78,152-159. Available at: http://ipnpr.jpl.nasa.gov/progress_report/42-78/78N.PDF (accessed on 4 May 2018), 1984.

Li, X.; Dick, G.; Ge, M.; Heise, S.; Wickert, J.; Bender, M. Real-time GPS sensing of atmospheric water vapor: Precise point positioning with orbit, clock, and phase delay corrections. Geophysical Research Letters, 41(10): 3615-3621, doi: 10.1002/2014jd021486, 2014.

Li, X.; Zus, F.; Lu, C.; Dick, G.; Ning, T.; Ge, M.; Schuh, H. Retrieving of atmospheric parameters from multi-GNSS in real time: validation with water vapor radiometer and numerical weather model. Journal of Geophysical Research: Atmospheres, 120(14): 7189-7204, doi: 10.1002/2015jd023454, 2015.

Lindskog, M.; Ridal, M.; Thorsteinsson, S.; Tong, N. Data assimilation of GNSS Zenith Total Delays from a Nordic processing centre. Atmospheric Chemistry & Physics, 17(22):1-22, doi: 10.5194/acp-2017-567, 2017.

Lu, C.; Li, X; Nilsson, T.; Ning, T.; Heinkelmann, R; Ge, M.; Schuh, H.. Real-time retrieval of precipitable water vapor from GPS and BeiDou observations. Journal of Geodesy, 89(9), 843-856, doi: 10.1007/s00190-015-0818-0, 2015.

Mlawer, J.; Taubman, J.; Brown, D.; Iacono, J.; Clough, A. Radiative transfer for inhomogeneous atmospheres: RRTM, a validated correlated‐k model for the longwave. Journal of Geophysical Research Atmospheres, 102(D14):16663-16682, doi: 10.1029/97JD00237, 1997.

Moeller, G.; Wittmann; C.; Yan, X.; Weber, R. GNSS tomography and assimilation test cases during the 2013 Central Europe floods. EGU General Assembly Conference, Vienna, Austria, 17-22 April 2016.

Monin, S.; Obukhov, M. Basic laws of turbulent mixing in the surface layer of the atmosphere. Contrib. Geophys. Inst. Acad. Sci. USSR., 64:1963-1987. Available at: https://www.mcnaughty.com/keith/papers/Monin_and_Obukhov_1954.pdf (accessed on 4 May 2018), 1954.

Nakamura, H.; Koizumi, K.; Mannoji, N.; Data assimilation of GPS precipitable water vapor into the JMA mesoscale numerical weather prediction model and its impact on rainfall forecasts. Journal of the Meteorological Society of Japan. Ser. II, 82(1B): 441-452, doi: 10.2151/jmsj.2004.441,2004.

401 Niell, E. Global mapping functions for the atmosphere delay at radio wavelengths. J. Geophys. Res., 101, doi:
402 3227-3246, 10.1029/95jb03048, 1996.

403 Nilsson, T.; Gradinarsky, L. Water vapor tomography using GPS phase observations: simulation results. IEEE
404 Transactions on Geoscience and Remote Sensing, 44(10): 2927-2941, doi: 10.1109/TGRS.2006.877755,
405 2006.

406 Pacione, R.; Sciarretta, C.; Faccani, C.; Ferretti, R.; Vespe, F. GPS PW assimilation into MM5 with the
407 nudging technique. Physics & Chemistry of the Earth Part A Solid Earth & Geodesy, 26(6-8):6-8,
408 doi:10.1016/S1464-1895(01)00088-6, 2001.

409 Perler, D.; Geiger, A.; Hurter, F. 4D GPS water vapor tomography: new parameterized approaches. Journal of
410 Geodesy, 85(8): 539-550, doi: 10.1007/s00190-011-0454-2, 2011.

411 Perler, D.; Geiger, A.; Rothacher, M. Determination of the 4D-Tropospheric Water Vapor Distribution by
412 GPS for the Assimilation into Numerical Weather Prediction Models. AGU Fall Meeting, San
413 Francisco ,USA, 5-9 December 2011.

414 Rocken, C.; Ware, R.; Van Hove, T.; Solheim, F.; Alber, C.; Johnson, J.; Solheim, F.; Alber, C.; Johnson, J.
415 Sensing atmospheric water vapor with the global positioning system. Geophys. Res. Lett., 20, 2631-2634, doi:
416 10.1029/93gl02935, 1993.

417 Rohm, W.; Bosy, J. The verification of GNSS tropospheric tomography model in a mountainous area.Adv.
418 Space Res., 47, 1721-1730, doi: 10.1016/j.asr.2010.04.017, 2011.

419 Saastamoinen, J. Atmospheric correction for the troposphere and stratosphere in radio ranging of satellites.
420 Use Artif. Satell. Geod., 15, 247-251, doi: 10.1029/GM015p0247, 1972.

421 Seko, H.; Shimada, S.; Nakamura, H.; Kato, T. Three-dimensional distribution of water vapor estimated from
422 tropospheric delay of GPS data in a mesoscale precipitation system of the Baiu front. Earth Planets & Space,
423 52(11):927-933, doi: 10.1186/bf03352307, 2000.

424 Shoji, Y.; Sato, K.; Yabuki, M.; Tsuda, T. PWV Retrieval over the ocean using shipborne GNSS receivers
425 with MADOCA real-time orbits. SOLA, 12: 265-271, doi: 10.2151/sola.2016-052, 2016.

426 Singh, S.; Mandal, M.; Bhaskaran, K. Impact of radiance data assimilation on the prediction performance of
427 cyclonic storm SIDR using WRF-3DVAR modelling system. Meteorology & Atmospheric Physics. (2):1-18,
428 doi:10.1007/s00703-017-0552-7, 2017.

429 Tewari, M.; Chen, F.; Wang, W.; Dudhia, J.; LeMone, A.; Mitchell, K.; Cuenca, H. Implementation and
430 verification of the unified noah land surface model in the WRF model. In Bulletin of the American
431 Meteorological Society., 2165-2170, doi:10.1007/s11269-013-0452-7, 2004.

432 Tregoning. P.; Boers, R.; O'Brien. D; Hendy, M. Accuracy of absolute precipitable water vapor estimates
433 from GPS observations. Journal of Geophysical Research: Atmospheres, 103(D22): 28701-28710, doi:
434 10.1029/98JD02516, 1998.

435 Vedel, H.; Huang, X. Impact of ground based GPS data on NWP forecasts. Journal of the Meteorological
436 Society of Japan, 82, 459-472, doi: 10.2151/jmsj.2004.459, 2004.

437 Wang, X.; Wang, X.; Dai, Z.; Ke, F.; Cao, Y.; Wang, F.; Song, L. Tropospheric wet refractivity tomography
438 based on the BeiDou satellite system. Advances in Atmospheric Sciences, 31(2), 355-362, doi:
439 10.1109/TGRS.2006.877755, 2014.

Wang, X., Dai, Z., Zhang, E., Fuyang, K. E., Cao, Y., Song, L.; Lianchun, S. Tropospheric wet refractivity tomography using multiplicative algebraic reconstruction technique. Advances in Space Research, 53(1), 156-162, doi: 10.1016/j.asr.2010.04.017, 2014.

Wexler, A. Vapor Pressure Formulation for Ice. Journal of Research of the National Institute of Standards-A. Physics and Chemistry, 81A(1): 5-20, doi: 10.6028/jres.081A.003, 1977.

Wexler, A. Vapor Pressure Formulation for Water in Range 0 to f 00 °C. A Revision. Journal of Research of the national Institute of Standards-A. Physics and Chemistry., 80A(5-6): 775-785, doi: 10.6028/jres.080A.071, 1976.

Yao, Y.; Zhang, B.; Xu, C.; Yan, F. Improved one/multi-parameter models that consider seasonal and geographic variations for estimating weighted mean temperature in ground-based GPS meteorology. Journal of Geodesy, 88(3):273-282, doi: 10.1007/s00190-013-0684-6, 2014.

Yuan, Y.; Zhang, K.; Rohm, W.; Choy, S.; Norman, R.; Wang, S. Real-time retrieval of precipitable water vapor from GPS precise point positioning. Journal of Geophysical Research: Atmospheres, 119(16): 10044-10057, doi: 10.1002/2014jd021486, 2014.

Zhang, B.; Fan, Q.; Yao, Y.; Li, X. An Improved Tomography Approach Based on Adaptive Smoothing and Ground Meteorological Observations. Remote Sensing, 9(9):886, doi: 10.3390/rs9090886, 2017.

Zhao, Q.; Yao, Y. An improved troposphere tomographic approach considering the signals coming from the side face of the tomographic area. Annales Geophysicae , 35(1): 87-95, doi: 10.5194/angeo-35-87-2017, 2017.